ACS APPLIED MATERIALS & INTERFACES

Research Article

Cite This: ACS Appl. Mater. Interfaces 2019, 11, 21526−21535

www.acsami.org

Three-dimensional Composite Catalysts for Al−O_2 Batteries Composed of $CoMn_2O_4$ Nanoneedles Supported on Nitrogen-Doped Carbon Nanotubes/Graphene

Yisi Liu,*[,†] Faqi Zhan,[‡] Biqiong Wang,[§] Bo Xie,[†] Qian Sun,[§] Hao Jiang,[∥] Jie Li,[⊥] and Xueliang Sun*[,§]

[†]Institute of Advanced Materials, Hubei Normal University, Huangshi 415000, China

[‡]State Key Laboratory of Advanced Processing and Recycling of Non-Ferrous Metals, Lanzhou University of Technology, Lanzhou 730050, China

[§]Department of Mechanical and Materials Engineering, University of Western Ontario, London, Ontario N6A 5B9, Canada

[∥]College of Materials and Chemical Engineering, Hunan City University, Yiyang 413000, China

[⊥]School of Chemistry and Chemical Engineering, Central South University, Changsha 410083, China

Supporting Information

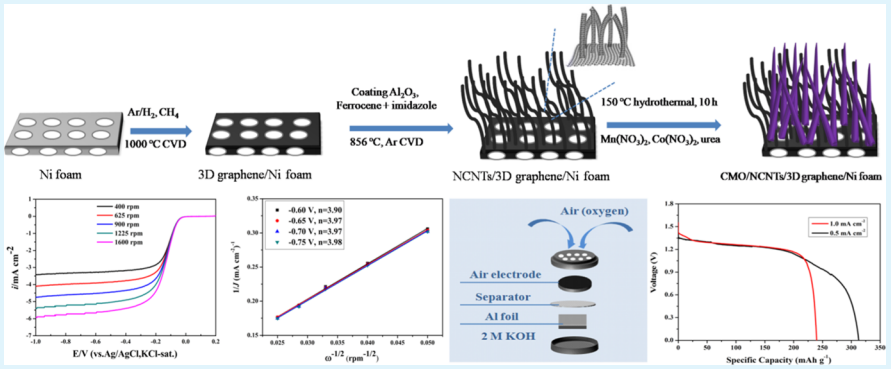

ABSTRACT: Great efforts have been focused on studying high-efficiency and stable catalysts toward oxygen reduction reaction (ORR) in metal−air batteries. In view of synergistic effects and improved properties, carbon nanotubes and three-dimensional graphene (CNTs-3D graphene) hybrid catalysts developed via a well-controlled route are urgently required. Herein, a $CoMn_2O_4$ (CMO) nanoneedle-supported nitrogen-doped carbon nanotubes/3D graphene (NCNTs/3D graphene) composite was prepared by in situ chemical vapor deposition (CVD) along with hydrothermal methods over a Ni foam substrate. The cyclic voltammetry and linear sweep voltammograms results indicate that the CMO/NCNTs/3D graphene hybrid possesses remarkable electrocatalytic performance toward ORR in alkaline conditions compared with NCNTs/3D graphene, CMO/3D graphene, and 3D graphene catalysts, even outperforming the commercial 20 wt % Pt/C catalyst. Moreover, the Al−air coin cell employing CMO/NCNTs/3D graphene as cathode catalysts obtains an open circuit voltage of 1.55 V and a specific capacity of 312.8 mA h g^{-1}, which are superior to the Al−air coin cell with NCNTs/3D graphene as catalysts. This work supplies new insights to advanced electrocatalysts introducing NCNTs/3D graphene as a catalyst support to develop scalable transition-metal oxide/NCNTs/3D graphene hybrids with excellent catalytic activity toward ORR in Al−air systems.

KEYWORDS: *aluminum−air coin cells, chemical vapor deposition, oxygen reduction reaction, nitrogen-doped carbon nanotubes, 3D graphene*

1. INTRODUCTION

Growing demand for energy leads to the rapid consumption of fossil fuels and intensifies the outbreak of environmental problems. The pressure from energy and environment greatly drives people to seek efficient and renewable energy storage and transformation technologies.[1,2] Recently, metal−air batteries have been comprehensively studied because of their two to ten times higher theoretical energy densities than state-of-the-art Li-ion batteries.[3] Particularly, Al−air batteries stand out from various metal−air batteries and are recognized as "green energy for the 21st century" because of their characteristics of higher theoretical voltage and energy density, lower price, security, and excellent stability.[4−7] In addition, aluminum is a cheap, abundant, recyclable, and environment-

Received: March 19, 2019
Accepted: May 28, 2019
Published: May 28, 2019

DOI: 10.1021/acsami.9b04861
ACS Appl. Mater. Interfaces 2019, 11, 21526−21535

friendly metal.[8] Oxygen reduction reaction (ORR) is the most important cathode process of the Al−air system, but its sluggish kinetics restricts the efficiency and performance of Al−air batteries.[9,10] Noble metal-based materials are regarded as the most outstanding ORR catalysts,[11,12] but the valuableness and terrestrial scarcity seriously obstruct their large-scale applications. Hence, it is highly desirable to explore high-efficiency nonprecious metal catalysts to solve the issues for advanced Al−air batteries.

Nowadays, three-dimensional (3D) carbon nanomaterials for electrocatalysis have gained more attention because of their high specific surface area, good mechanical integrity, and facilitated ion diffusion/charge transfer paths.[13−16] Thereinto, 3D graphene possesses great advantages, such as high electronic conductivity, excellent chemical stability, and so forth, which are widely utilized in electrocatalysis.[15,17,18] For example, Wang et al.[17] proved that few-layer 3D graphene could be regarded as a high-efficiency electrocatalyst toward ORR. Xue et al.[19] reported that 3D B, N codoped graphene foams prepared by a modified chemical vapor deposition (CVD) method could be used as highly efficient ORR catalysts. In addition, CNTs are also regarded as excellent catalyst supports[20−23] in metal−air systems due to their high tensile modulus, high specific surface area, mesoporous structure, and good electrical properties. Zhao et al.[23] prepared spinel $MnCo_2O_4$ nanoparticles partly imbedded in N-doped CNTs and discovered their high ORR and OER catalytic performances, even surpassing the activity of Pt/C, RuO_2, and IrO_2 bifunctional catalysts in metal−air batteries. The enhanced catalytic activity is contributed to the synergetic effect from the nitrogen groups in the NCNTs and the spinel Mn−Co oxide particles.

Incorporating 1D CNTs into 3D graphene to prepare CNT-graphene hybrids with interconnected architecture is one promising direction for electrocatalytic research, considering that the 3D structure and synergistic effects can prevent aggregation and enhance the stability of electrocatalysts. This design allows for larger accessible porous structures and controllable modifications such as the introduction of appropriate dopants (N, P, S, etc.) to further improve electrocatalytic activity.[24,25] In numerous candidate dopants, N is considered to be an outstanding element for the chemical doping of carbon materials because its atomic size is similar to C, and the lone pair electrons can form the delocalized conjugated system with the carbon skeleton of sp^2 hybridization,[26] which produces more active sites because of its spin density, charge distribution, and electronic state density change.[27] Ma et al.[24] synthesized a three-dimensional composite catalyst (NCNTs/G) of NCNTs grown on graphene by the pyrolysis of pyridine on a Ni substrate, which exhibited high electrocatalytic activity and selectivity toward ORR under alkaline conditions, indicating its potential application in fuel cells. Ratso et al.[28] reported a nitrogen-doped nanocarbon catalyst (FLG/MWCNT) that showed improved catalytic performance toward ORR in alkaline conditions comparable with the commercial Pt/C catalyst induced by a higher content of nitrogen doping. The 3D NCNT−graphene hybrid has been extensively studied as an alternative support toward ORR. Furthermore, CNT−graphene functionalized with inorganic nanocrystals (transition metal,[29] metal oxides,[30,31] sulfides,[32,33] nitrides,[2] and carbides[34]) show synergistic effects and significant improvement in electrocatalysis.

In this work, a composite of $CoMn_2O_4$ nanoneedles supported on NCNTs/3D graphene was synthesized by optimized CVD and hydrothermal processes. The CMO/NCNTs/3D graphene hybrid catalyst has a robust and well-developed hierarchical porous structure. The combination of the unique architecture with abundant C−N active sites and M−N species enables the catalyst to exhibit excellent catalytic performance toward ORR in alkaline conditions, and superior stability and methanol tolerance compared with the commercial Pt/C catalyst. An Al−air coin cell was assembled with the CMO/NCNTs/3D graphene hybrid as the cathode catalyst and exhibited an open-circuit voltage of 1.55 V and a specific capacity of 312.8 mA h g^{-1} at a discharge current density of 1.0 mA cm^{-2}.

2. EXPERIMENTAL SECTION

2.1. Preparation of 3D Graphene. 3D graphene was synthesized by a single-step CVD method. A piece of Ni foam was placed on a clean alumina boat in the center of a quartz tube. Vacuum grease was used to make sure that the quartz tube was completely sealed against ambient air. The quartz tube was purged by Ar and H_2 gases with 100:10 sccm for 15 min. Then, the furnace temperature was set to 1000 °C for at least 15 min to ensure all potential surface contaminants and oxide layer are reduced and removed from the substrate surface. Next, CH_4 gas was applied at 15−20 sccm for 90 min, while keeping Ar and H_2 running. Afterward, the furnace was closed and gradually cooled down to room temperature with Ar and H_2 running.

2.2. Preparation of NCNTs/3D Graphene. Nitrogen-doped carbon nanotubes (NCNTs) were synthesized by the floating catalyst CVD (FCCVD). The Al_2O_3 layer was coated by atomic layer deposition (ALD). To assist with the growth of vertical NCNTs, an Al_2O_3 layer was initially deposited on the surface of as-prepared graphene/Ni foam using ALD. Before the tube furnace started running, high-purity Ar gas was imported to the tube for 0.5 h to purge out the air of the system. Imidazole (2.0 g) and ferrocene (0.2 g) were separately dissolved in 10 mL of acetonitrile to be used as the carbon source and catalyst precursor, respectively. When the temperature reached 856 °C, the ferrocene and imidazole solutions were in turn sprayed onto graphene. The synthesis time was 5 min. The Ar gas flow was fixed to 60 sccm during the whole process.

2.3. Preparation of the $CoMn_2O_4$ Nanoneedles Supported on Nitrogen-Doped Carbon Nanotubes Grown on the 3D Graphene (CMO/NCNTs/3D Graphene) Hybrid. In the typical synthesis of the CMO/NCNTs/3D graphene hybrid, 0.5 mmol $Co(NO_3)_2{\cdot}6H_2O$, 1 mmol $Mn(NO_3)_2{\cdot}4H_2O$, and 30 mmol urea were ultrasonically dispersed in a mixture of 20 mL of ethanol and 20 mL of deionized water, and transferred into a 50 mL Teflon-lined autoclave; then, a piece of NCNTs/3D graphene was immersed into the solution and heated at 150 °C for 10 h. The product was collected and washed by centrifuging with deionized water and ethanol several times. The as-prepared CMO/NCNTs/3D graphene with Ni was immersed in 3 M HCl solution at room temperature to etch the Ni scaffold. CMO/3D graphene was synthesized using the same process without growing NCNTs. In order to make a complete contrast, the mechanical mixture of CMO, NCNTs, and 3D graphene was prepared by ball-milling.

2.4. Fabrication of Aluminum−Air Coin Cells. The detail procedures of fabrication were described in the Supporting Information as our previous work reported.[61] Al foils, glass microfibers, and KOH solution were used as the anode, the separator, and the electrolyte, respectively.

2.5. Materials Characterization. Detailed measurement requirements of field emission scanning electron microscopy (FESEM), high-resolution transmission electron microscopy (HRTEM), Raman spectra, X-ray photoelectron spectroscopy, and nitrogen adsorption−desorption isotherm measurements are described in the Supporting Information.

DOI: 10.1021/acsami.9b04861
ACS Appl. Mater. Interfaces 2019, 11, 21526−21535

Scheme 1. Schematic Illustration for the Synthesis of the CNTs/3D Graphene and CMO/CNTs/3D Graphene Hybrids

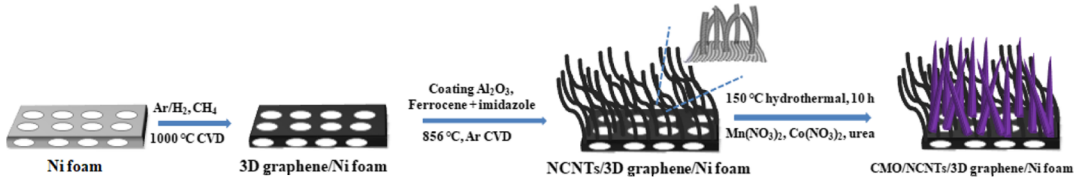

2.6. Electrochemical Measurements. The electrochemical characterizations were operated in a standard three-electrode system at room temperature using a rotating disk electrode setup with a Pine bipotentiostat and rotation controller. The Pt wire and Ag/AgCl (3 M KCl) served as the counter and reference electrodes, respectively. The electrolyte was 0.1 M KOH solution. The process of catalyst ink preparation and test methods were reported as our previous work[30,35] (Supporting Information).

3. RESULTS AND DISCUSSIONS

3.1. Physical Characterizations. The synthesis strategy of NCNTs/3D graphene and CMO/NCNTs/3D graphene hybrids were schematized in Scheme 1. At 856 °C, ferrocene decomposed into iron as the catalyst for NCNT growth. Al_2O_3 coating can create a rough surface that absorbs iron atoms into the traps of the alumina layer and forms homogeneous and well-dispersed catalytic particles to obtain uniform and high-density NCNTs.[58]

The X-ray diffraction (XRD) patterns of CNTs/3D graphene, CMO/3D graphene, and CMO/CNTs/3D graphene hybrids are shown in Figure 1. The characteristic

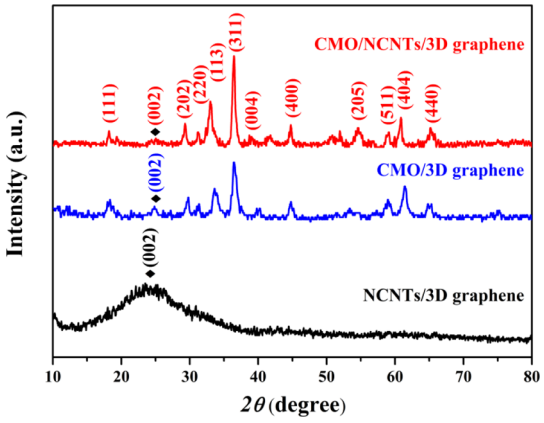

Figure 1. XRD spectra of the CNTs/3D graphene, CMO/3D graphene, and CMO/CNTs/3D graphene hybrids, respectively.

diffraction peaks of CMO/3D graphene and CMO/CNTs/3D graphene hybrids were indexed to crystal planes of tetragonal $CoMn_2O_4$ (JCPDS: 18-0408). The characteristic peak of graphite at 25.3° (002) was observed in all the samples, indicating that $CoMn_2O_4$ nanocrystals are efficiently deposited on the CNTs/3D graphene.

As shown in the SEM images of 3D graphene/Ni foam (Figure S1), the continuously wrinkled graphene network was decorated on Ni foam with a macroporous structure. The SEM images of NCNTs/3D graphene (Figures S2a and 2a) show that well-defined NCNTs of approximately 50 μm in length and 50 nm in diameter were grown on the 3D graphene surface with high density in a stable linkage, constructing a porous 3D interconnected carbon skeleton, facilitating fast reactant diffusion and rapid electron transfer. As shown in Figure S2b, intensive CMO nanoneedles were uniformly grown on the 3D graphene surface with high density. For CMO/NCNTs/3D graphene, CMO nanoneedles were intertwined with NCNTs (Figure 2b). The energy-dispersive X-ray mapping images of a selective region (Figure 2c) reveal the existence and uniform distribution of Mn (0.07 at. %), Co (0.12 at. %), Ni (9.10 at. %), C (77.29 at. %), and O (13.43 at. %) elements, further demonstrating the possibility of $CoMn_2O_4$ formation.

TEM images of NCNTs/3D graphene (Figure 3a,b) display that NCNTs have bamboo-like structures and are vertically grown on 3D graphene with high density. Figure S3a clearly indicated the bonding between NCNTs and graphene. The black dots are Fe nanoparticles as catalysts on the top of NCNTs for terminal growth of NCNTs. They cannot be completely etched by HCl solution, and they would not participate in ORR. Remarkably, the bamboo-like NCNTs could supply more graphene edges so that abundant ORR active sites were introduced.[24] As shown in Figures 3c,d and S1, CMO nanoneedles with a length of ~500 nm were intertwined together with NCNTs and distributed randomly on 3D graphene. CMO nanoneedles were further observed by HRTEM measurement (Figure 4a,b), which were composed of a plurality of CMO cubic nanoparticles of about 10 nm. The lattice fringes with spacings of 0.246 and 0.285 nm correspond to the (311) and (220) planes of the tetragonal $CoMn_2O_4$ structure, which were consistent with XRD results. The unique structure gives more effectively exposed activity sites and greater accessibility of oxygen to catalyze the ORR.

The structural composition and defectiveness were further evaluated by Raman spectroscopy (Figure 5a). Two representative peaks at 1590 and 2750 cm^{-1} are detected for all samples, corresponding to the G band and 2D band of carbon materials, respectively. The G band corresponds to the doubly degenerate E_{2g} phonons at the Brillouin zone center.[55] The D band is attributed to the breathing mode of sp^2 rings and requires a defect for its activation by an intervalley double-resonance (DR) Raman process.[36] The 2D band is due to the same second-order, intervalley DR process, but no defects are required for its activation.[36] No obvious D band was observed for 3D graphene and NCNTs/3D graphene, indicating a well-ordered graphitic structure and low defect degree. CMO nanoneedles can induce more oxygen-containing functional groups and surface defects. The emerging weak D band for CMO/CNTs/3D graphene demonstrates increased significant defects, resulting in more active sites for electrocatalytic activity. Additionally, the peaks observed between 400 and 700 cm^{-1} can be attributed to the functional groups containing Mn−O and Co−O.[59]

The XPS survey spectrum of CMO/CNTs/3D graphene after the etching treatment reveals the presence of C (71.21 at. %), N (1.22 at. %), Co (2.62 at. %), Mn (1.76 at. %), and O (23.19 at. %) without any other impurity in the sample, whereas that of the CMO/3D graphene hybrid presents four

DOI: 10.1021/acsami.9b04861
ACS Appl. Mater. Interfaces 2019, 11, 21526−21535

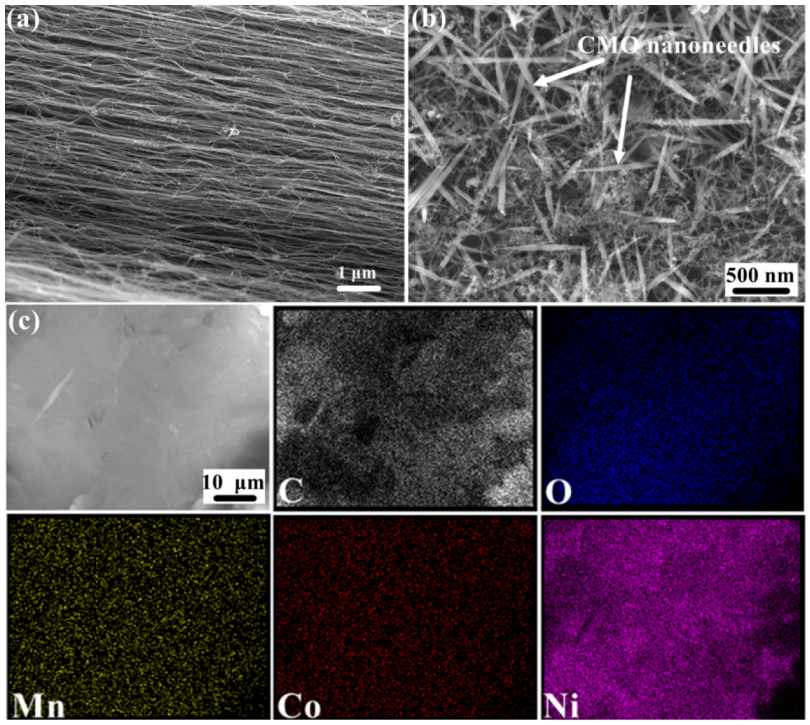

Figure 2. FESEM image of (a) NCNTs/3D graphene hybrid and (b) CMO/NCNTs/3D graphene hybrid; (c) elemental mapping images of C, O, Mn, Co, and Ni in the CMO/NCNTs/3D graphene hybrid.

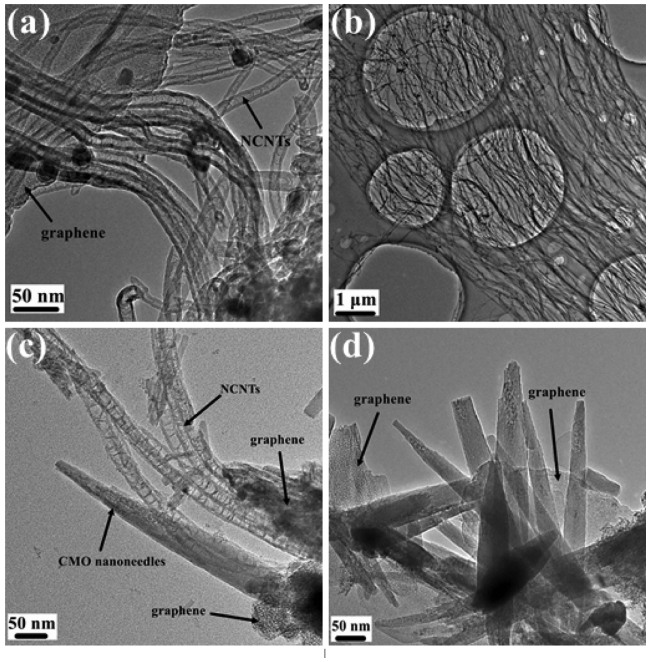

Figure 3. TEM images of (a,b) NCNTs/3D graphene and (c,d) CMO/NCNTs/3D graphene in different regions, respectively.

elements: C (58.78 at. %), O (35.75 at. %), Co (3.50 at. %), and Mn (1.97 at. %) (Figure 5b). In the C 1s high-resolution spectrum (Figure 5c), four obvious peaks belonging to C−C (sp^2), C−N, C═O, and O−C═O groups are observed.[37] The high-resolution N 1s spectrum (Figure 5d) can be deconvoluted into four peaks centered at 398.4, 399.1, 400.0, and 404.1 eV, which are attributed to pyridinic N, pyrrolic N, graphitic N, and pyridinic N oxide, respectively (Figure 5d).[38] It is well known that the predominant graphitic N has an active

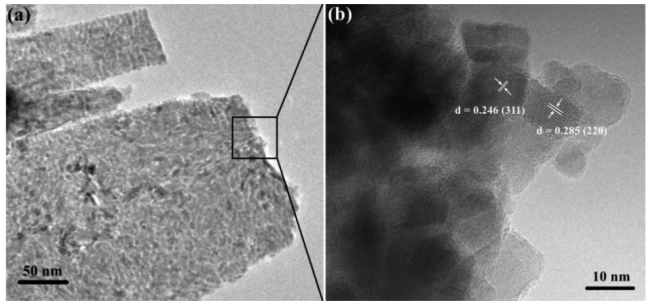

Figure 4. (a) TEM and (b) HRTEM images of CMO nanoneedles.

effect in promoting catalytic activity toward ORR.[38,39] The electronegativity of graphitic N atoms reduces the electron density of adjacent C atoms which is conductive to transferring electrons from C atoms to N atoms and feedback electrons from N atoms to p_z orbitals of adjacent C atoms.[40−42] Pyrrolic N is generally located at the edge site with intrinsic activity.[60] The high-resolution Co 2p spectrum (Figure 5e) is composed of two pairs of spin−orbit peaks, demonstrating the coexistence of Co(II) and Co(III).[43] The high-resolution Mn 2p spectra show two peaks at 642.24 and 654.19 eV, which belong to the binding energies of $2p_{3/2}$ and $2p_{1/2}$, respectively (Figure 5f). The energy interval between $2p_{3/2}$ and $2p_{1/2}$ is 11.9 eV, conforming to the characteristic of valence fluctuation of Mn.[44,45] The Mn 2p spectrum contains two doublets: the strongest doublet of 644.94 and 656.64 eV belongs to Mn(IV), and the second doublet of 642.14 and 653.84 eV is attributed to Mn(III). The redox of Mn species can be regarded as an assistor in charge transfer.[56,57] The O 1s spectrum (Figure S5) reveals three oxygen states: oxygen in $CoMn_2O_4$, the absorbed oxygen species, and the residual oxygen-containing groups of NCNTs/3D graphene.[46] Comparing with Mn 2p and Co 2p spectra of CMO/3D graphene (Figure S6), the binding energy

DOI: 10.1021/acsami.9b04861
ACS Appl. Mater. Interfaces 2019, 11, 21526−21535

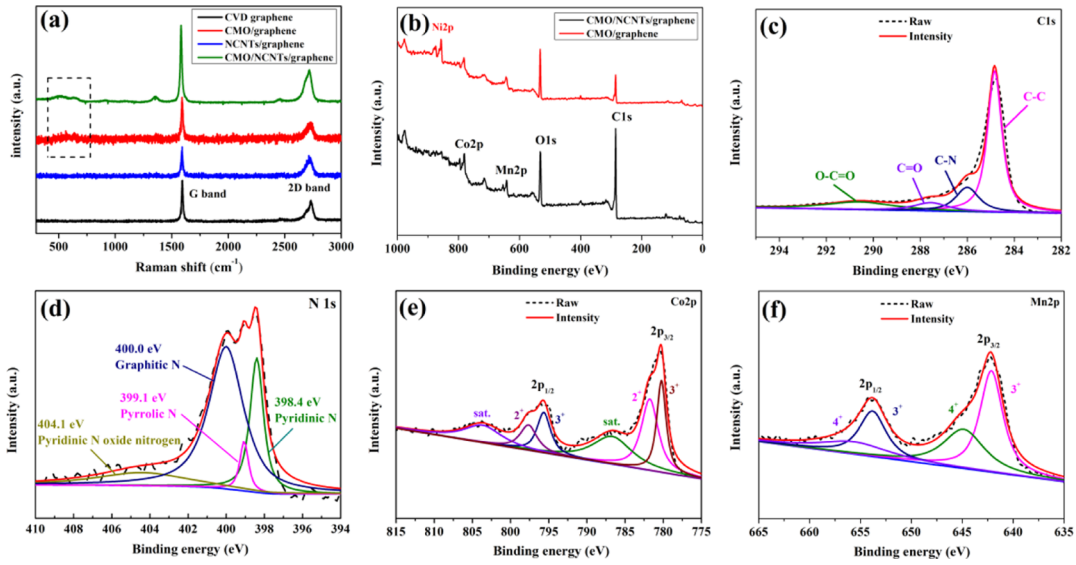

Figure 5. (a) Raman spectra of the 3D graphene, CMO/3D graphene, NCNTs/3D graphene, and CMO/NCNTs/3D graphene hybrids, respectively. The laser excitation wavelength is 532 nm; (b) XPS spectra of CMO/3D graphene and CMO/NCNTs/3D graphene hybrid; high-resolution XPS spectra of CMO/NCNTs/3D graphene: (c) C 1s, (d) N 1s, (e) Co 2p, and (f) Mn 2p, respectively.

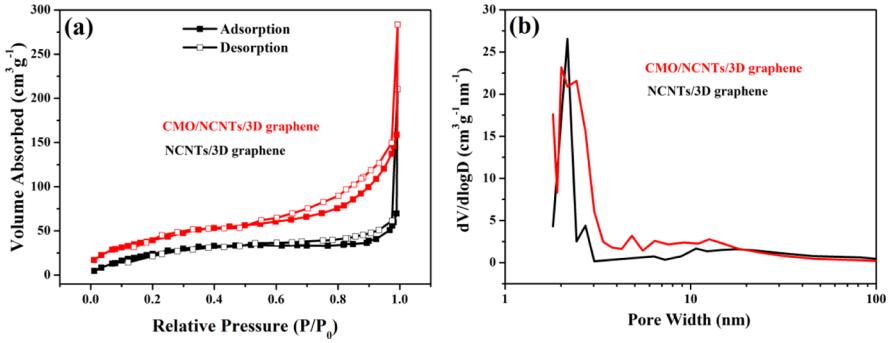

Figure 6. (a) N_2 adsorption−desorption isotherm and (b) BJH absorption pore size distribution of the NCNTs/3D graphene and CMO/NCNTs/3D graphene hybrids, respectively.

of Mn 2p and Co 2p for the CMO/NCNTs/3D graphene hybrid shift toward lower energy direction, probably as a result of the combination between M and N,[47] producing M−N_x−C active sites. The M−N_x functional groups in the carbon matrix are considered as the active sites, which can facilitate the dissociation of O_2 and desorption of H_2O in the ORR process.[48,49]

A high surface area (S_{BET}) and hierarchically porous structure can provide more active sites and efficient mass transport, and bring out a better electrocatalytic activity toward ORR.[50,51] The N_2 adsorption−desorption isotherms for the NCNTs/3D graphene and CMO/NCNTs/3D graphene hybrids are shown in Figure 6. They both present type IV isotherms with H4 hysteresis, suggesting the coexistence of mesopores and macropores.[52,53] The calculated S_{BET} and average pore diameter are 111.9 $m^2 \cdot g^{-1}$ and 13.43 nm for NCNTs/3D graphene and 148.4 $m^2 \cdot g^{-1}$ and 12.9 nm for CMO/NCNTs/3D graphene, respectively. The higher specific surface area of CMO/NCNTs/3D graphene provides more active sites leading to improved catalytic activity. These mesopores and macropores are helpful to ensure efficient exposure of active sites and mass transport in the process of ORR catalysis.[33]

3.2. Electrocatalytic Performance of the Electrocatalysts for ORR. Figure 7a compares the cyclic voltammograms of graphene, CMO/3D graphene, NCNTs/3D graphene, mechanical mixture, and CMO/NCNTs/3D graphene catalysts in O_2-saturated 0.1 M NaOH aqueous solution. The voltammetric features of all the catalysts reveal the typical oxygen reduction peaks in the region between −0.1 and −0.4 V (vs Ag/AgCl), indicating their ORR catalytic activity. CMO/NCNTs/3D graphene exhibits a more positive ORR peak potential of −0.20 V compared to NCNTs/3D graphene (−0.29 V), CMO/3D graphene (−0.29 V), mechanical mixture (−0.28 V), and 3D graphene (−0.35 V), suggesting CMO/NCNTs/3D graphene has better electrocatalytic activity. Additionally, linear sweep voltammograms (LSVs) with a rotation rate of 1600 rpm in O_2-saturated 0.1 M KOH were measured to further study the ORR catalytic kinetics (Figure 7b). It is observed that CMO/NCNTs/3D graphene has an onset potential (E_{onset}) of −0.07 V, which is more positive than that of NCNTs/3D graphene (−0.13 V), CMO/3D graphene (−0.12 V), mechanical mixture (−0.11 V), and 3D graphene (−0.16 V), demonstrating the higher catalytic activity of CMO/NCNTs/3D graphene. The half-wave potential ($E_{1/2}$) of CMO/NCNTs/3D graphene (−0.16 V) is more positive than the comparative catalysts, indicating its

DOI: 10.1021/acsami.9b04861
ACS Appl. Mater. Interfaces 2019, 11, 21526−21535

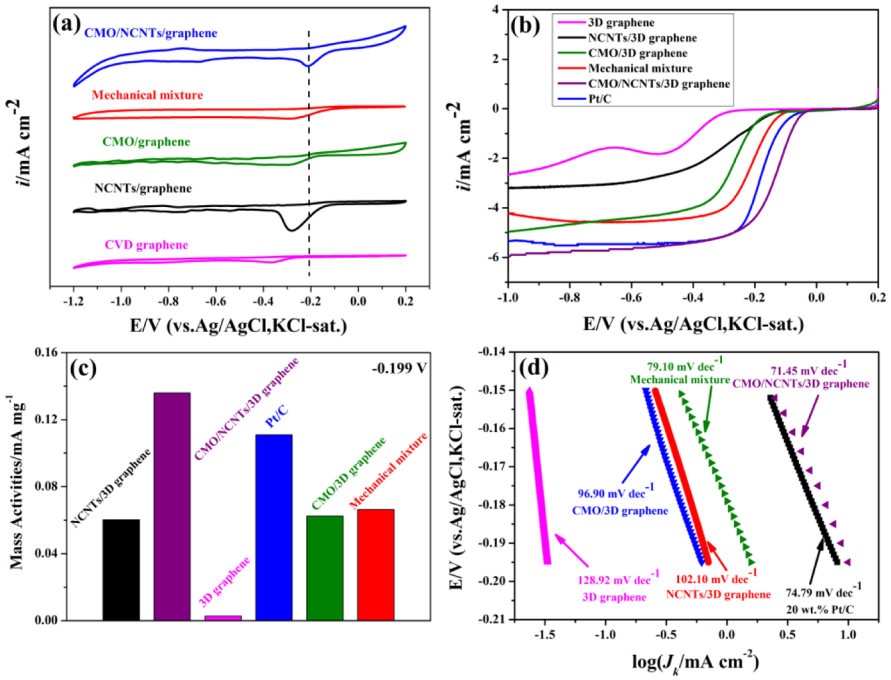

Figure 7. (a) Cyclic voltammograms of 3D graphene, CMO/3D graphene, NCNTs/3D graphene, mechanical mixture, and CMO/NCNTs/3D graphene electrocatalysts in O_2-saturated 0.1 M KOH aqueous solution, respectively; (b) LSV curves of 3D graphene, CMO/3D graphene, NCNTs/3D graphene, mechanical mixture, and CMO/NCNTs/3D graphene and 20 wt % Pt/C electrocatalysts on RDE electrode in O_2-saturated 0.1 M KOH solution at a rotation rate of 1600 rpm with a scan rate of 5 mV s^{-1}; (c) mass activities at −0.199 V for all catalysts; (d) Tafel slopes from LSV cures at 1600 rpm.

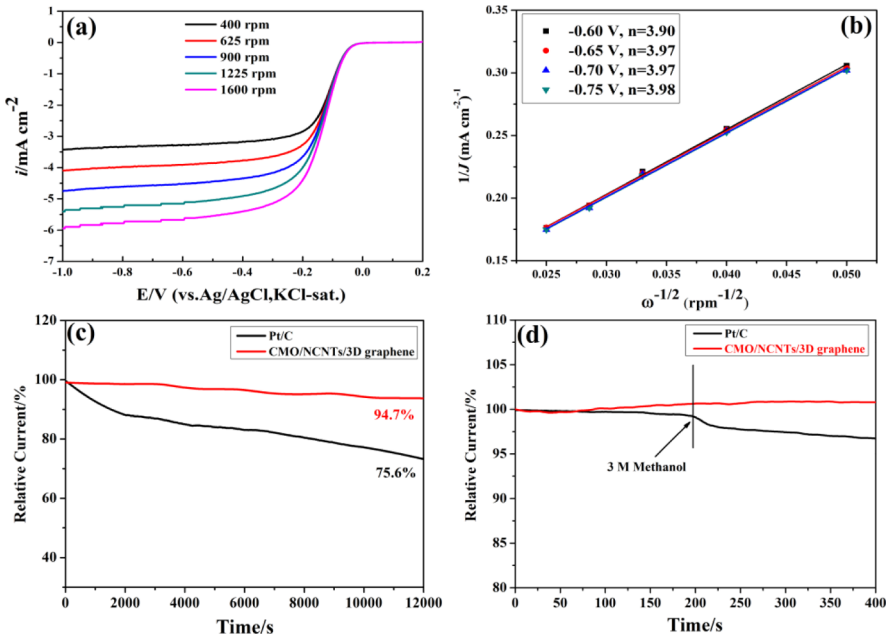

Figure 8. (a) LSV curves of the CMO/NCNTs/3D graphene hybrid in O_2-saturated 0.1 M KOH solution at various rotation rates with a scan rate of 5 mV s^{-1}; (b) corresponding Koutecky−Levich plots at different potentials; (c) current−time chronoamperometric response of Pt/C, CMO/NCNTs/3D graphene electrocatalysts at −0.30 V in O_2-saturated 0.1 M KOH solution; (d) chronoamperometric response of Pt/C and CMO/NCNTs/3D graphene electrocatalysts at −0.30 V in O_2-saturated 0.1 M KOH solution. The rotation rate is 900 rpm. The arrow indicates the introduction of 3 M methanol.

faster ORR kinetics resulting in better catalytic performance. Moreover, the current plateau for CMO/NCNTs/3D graphene represents a diffusion-controlled process corresponding to the efficient four-electron-dominated ORR pathway.[54] As observed from Figure 7c, CMO/NCNTs/3D graphene exhibits a Tafel slope of 71.45 mV dec^{-1} far less than NCNTs/3D graphene (102.10 mV dec^{-1}), mechanical mixture (79.10 mV dec^{-1}), CMO/3D graphene (96.90 mV dec^{-1}), and 3D graphene (128.92 mV dec^{-1}), and even surpassing the 20 wt % Pt/C catalyst (74.79 mV dec^{-1}), suggesting that CMO/NCNTs/3D graphene possesses faster reaction kinetics. Figure 7d displays obvious higher mass activity at −0.199 V for

DOI: 10.1021/acsami.9b04861
ACS Appl. Mater. Interfaces 2019, 11, 21526−21535

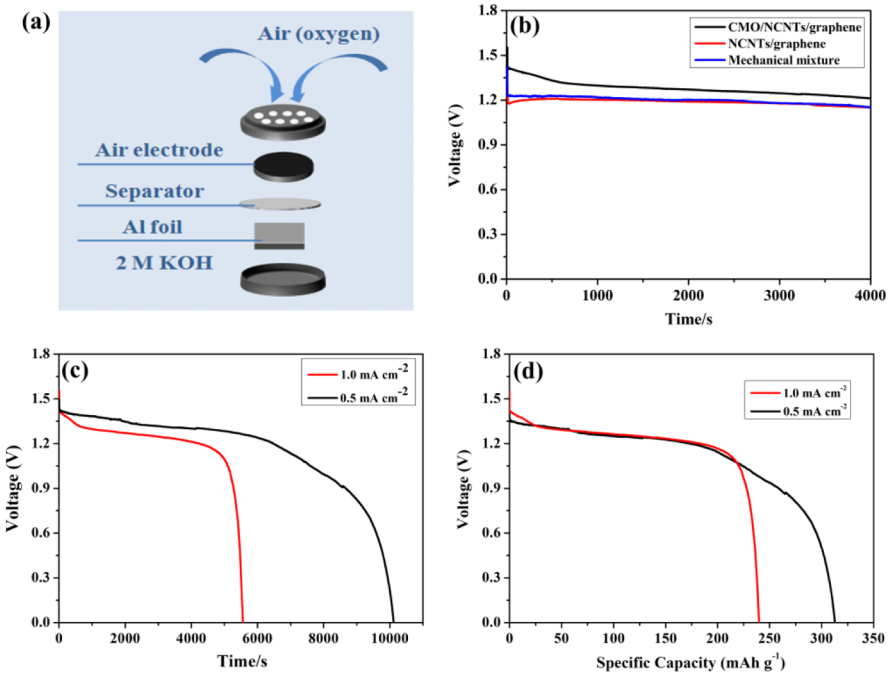

Figure 9. (a) Conformation of an Al−air coin cell; (b) discharge curves of the coin Al−air batteries with the CMO/NCNTs/3D graphene, NCNTs/graphene, and mechanical mixing electrocatalysts under ambient conditions at a current density of 1.0 mA cm^{-2}, respectively; (c,d) discharge curves for the Al−air coin cell with CMO/NCNTs/3D graphene at current densities of 0.5 and 1.0 mA cm^{-2}.

CMO/NCNTs/3D graphene (0.136 A mg^{-1}) compared with other catalysts, suggesting the best electrocatalytic activity. These results emphasized improved ORR catalytic activity of CMO/NCNTs/3D graphene, which could be ascribed to the synergetic effect from four aspects: (1) charge redistribution can be caused by introducing N into the graphitic skeleton to promote the adsorption of oxygen; (2) a small number of Mn and Co can form Mn−N and Co−N active centers and selectively accelerate the formation of N−C active sites; (3) the electronic interactions between 3D graphene and NCNTs, and between NCNTs/3D graphene and anchored CMO nanoneedles effectively improve the ORR catalytic performance; (4) the unique porous structure provides more accessible catalytic active sites and electron transfer pathways. The electrocatalytic properties are listed in Table S1. Furthermore, the outstanding ORR catalytic activity of CMO/NCNTs/3D graphene is comparable with or surpasses many recently reported 3D graphene or NCNTs based electrocatalysts in alkaline conditions (see Table S1).

ORR can proceed by two pathways in alkaline medium: direct four-electron reduction pathway and successive two-electron reduction pathway.[52] The electron transfer numbers (n) are calculated by Koutecky−Levich (K−L) equations (Supporting Information). The LSV curves with a serious of rotating rates and corresponding K−L plots at different potentials for the CMO/NCNTs/3D graphene hybrid were exhibited in Figure 8a,b. The calculated n of 3.96 is close to the Pt/C catalyst (4.0, Figure S7), indicating the high selectivity for 4e-reduction path. In addition, the n of CMO/NCNTs/3D graphene is larger than that of CMO/3D graphene (3.72, Figure S8), further demonstrating the significant effect of NCNTs on ORR catalytic activity.

The ORR long-term stability of CMO/NCNTs/3D graphene was comparatively investigated by the chronoamperometric method (Figure 8c). After 12 000 s of continuous operation at a constant voltage of −0.3 V, CMO/NCNTs/graphene showed an efficient current density retention rate of 94.7%, far higher than the Pt/C catalyst (75.6% retention), indicating improved ORR stability under alkaline conditions. The cycle stability of CMO/NCNTs/3D graphene was also investigated via CV tests for 3000 consecutive cycles (Figure S9). The LSV curve after 3000 CV cycles exhibits no obvious change of $E_{1/2}$ and a tiny decrease of diffusion-limiting current density, manifesting good stability of CMO/NCNTs/3D graphene. As shown in Figure 8d, to examine the methanol crossover effect, the chronoamperometric responses after adding 3 M methanol to the O_2-saturated 0.1 M KOH electrolyte were given. The ORR current density for CMO/NCNTs/3D graphene almost remains unchanged in contrast to the significant decrease for the Pt/C catalyst, which should be ascribed to incomplete methanol oxidation on CMO/NCNTs/3D graphene, demonstrating its higher tolerance ability against methanol.

3.3. Al−Air Coin Cell Performances. To further evaluate the applied electrocatalytic performance, novel Al−air coin cells (Figure 9a) were assembled, employing as-prepared catalysts. Figure 9b displays the discharge curves of coin cells at a current density of 1.0 mA cm^{-2} in atmospheric environment employing CMO/NCNTs/3D graphene, NCNTs/3D graphene, and the mechanical mixture as cathode catalysts. The coin cell with CMO/NCNTs/3D graphene as the electrocatalyst exhibits an open circuit voltage of 1.55 V and a flat plateau of 1.36 V, which is higher than those of NCNTs/3D graphene (1.38 and 1.21 V) and the mechanical mixture (1.42 and 1.23 V). Figure 9c,d, shows typical galvanostatic discharge curves at different current densities of 0.5 and 1.0 mA cm^{-2} for the coin cells with CMO/NCNTs/3D graphene as cathode catalysts. When the current density increased, the voltage plateau decreased in view of the more serious cell polarization. The specific capacities normalized to the mass of consumed Al

DOI: 10.1021/acsami.9b04861
ACS Appl. Mater. Interfaces 2019, 11, 21526−21535

are 239.8 and 312.8 mA h g^{-1} at the current densities of 0.5 and 1.0 mA cm^{-2}, respectively. The superior Al−air coin cell performance further confirm more excellent electrocatalytic activity of CMO/NCNTs/3D graphene, which is ascribed to the synergistic effect and the electronic interactions between 3D graphene and NCNTs, and between NCNTs/3D graphene and anchored CMO nanoneedles for ORR.

4. CONCLUSIONS

In summary, $CoMn_2O_4$ nanoneedles intertwined in the NCNTs/3D graphene hybrid were fabricated by in situ CVD and hydrothermal strategies. The CMO/NCNTs/3D graphene hybrid exhibits comparable electrocatalytic activity toward ORR with the commercial 20 wt % Pt/C catalyst but far outperforms its counterpart in the aspect of durability and methanol tolerance. These benefits can be attributed to the 3D interconnected network, the large specific surface area with high porosity, the exposure of $M-N_x$ moieties and C−N active sites, as well as the synergistic effect between CMO nanoneedles and NCNTs/3D graphene. The discharge performance of coin cells demonstrates the positive role of $M-N_x$ active sites derived from CMO and N species. Our work demonstrates the great potential of the CMO/NCNTs/3D graphene hybrid material as ORR electrocatalysts in Al−air batteries and would inspire more breakthroughs in the development of novel NCNTs/3D graphene-based electrocatalysts.

■ ASSOCIATED CONTENT

Supporting Information

The Supporting Information is available free of charge on the ACS Publications website at DOI: 10.1021/acsami.9b04861.

Fabrication of aluminum−air coin cells; materials characterization; electrochemical measurements; the K−L equation; SEM images of 3D graphene/Ni foam; SEM images of NCNTs/3D graphene and CMO/3D graphene; TEM images of CMO/NCNTS/3D graphene and CMO nanoneedles; high-resolution XPS spectra of O 1s for CMO/NCNTs/3D graphene; a comparison of high-resolution Mn 2p and Co 2p spectra for CMO/NCNTs/3D graphene and CMO/3D graphene; LSV curves and K−L plots of 20 wt % Pt/C and CMO/3D graphene; and the durability test of the CMO/NCNTs/3D graphene hybrid (PDF)

■ AUTHOR INFORMATION

Corresponding Authors

*E-mail: yliu88@hbnu.edu.cn. Phone: +86 18772289593 (Y.L.).

*E-mail: xsun@eng.uwo.ca (X.S.).

ORCID

Faqi Zhan: 0000-0003-1836-5211

Bo Xie: 0000-0002-3862-0411

Xueliang Sun: 0000-0003-2881-8237

Notes

The authors declare no competing financial interest.

■ ACKNOWLEDGMENTS

This study was supported by the Natural Sciences and Engineering Research Council of Canada, Canada Research Chair Program, the Scientific Research Project of Education Department of Hubei Province (no. 20182505), the Hubei Key Laboratory Analysis & Reuse Technology (Hubei Normal University, no. PA180103), and the National Nature Science Foundation of China (no. 51474255).

■ REFERENCES

(1) Eberle, D. U.; von Helmolt, D. R. Sustainable Transportation Based on Electric Vehicle Concepts: A Brief Overview. *Energy Environ. Sci.* **2010**, *3*, 689−699.

(2) Shen, M.; Wei, C.; Ai, K.; Lu, L. Transition metal-nitrogen-carbon nanostructured catalysts for the oxygen reduction reaction: From mechanistic insights to structural optimization. *Nano Res.* **2017**, *10*, 1449−1470.

(3) Dunn, B.; Kamath, H.; Tarascon, J.-M. Electrical Energy Storage for The Grid: A Battery of Choices. *Science* **2011**, *334*, 928−935.

(4) Li, Q.; Bjerrum, N. J. Aluminum as Anode for Energy Storage and Conversion: A Review. *J. Power Sources* **2002**, *110*, 1−10.

(5) Mori, R. Electrochemical properties of a rechargeable aluminum-air battery with a metal-organic framework as air cathode material. *RSC Adv.* **2017**, *7*, 6389−6395.

(6) Mokhtar, M.; Talib, M. Z. M.; Majlan, E. H.; Tasirin, S. M.; Ramli, W. M. F. W.; Daud, W. R. W.; Sahari, J. Recent developments in materials for aluminum-air batteries: A review. *J. Ind. Eng. Chem.* **2015**, *32*, 1−20.

(7) Zhang, Y.; Li, X.; Zhang, M.; Liao, S.; Dong, P.; Xiao, J.; Zhang, Y.; Zeng, X. IrO_2 Nanoparticles Highly Ddispersed on Nitrogen-Doped Carbon Nanotubes as An Efficient Cathode Catalyst for High-Performance Li-O_2 Batteries. *Ceram. Int.* **2017**, *43*, 14082−14089.

(8) Schwarz, H.-G. Aluminum Production and Energy. *Encyclopedia of Energy*; Elsevier, 2004; Vol. *1*, pp 81−95.

(9) Wang, Z.-L.; Xu, D.; Xu, J.-J.; Zhang, X.-B. Oxygen Electrocatalysts in Metal-Air Batteries: From Aqueous to Nonaqueous Electrolytes. *Chem. Soc. Rev.* **2014**, *43*, 7746−7786.

(10) Lee, J.-S.; Tai Kim, S.; Cao, R.; Choi, N.-S.; Liu, M.; Lee, K. T.; Cho, J. Metal-Air Batteries with High Energy Density: Li-Air versus Zn-Air. *Adv. Energy Mater.* **2011**, *1*, 34−50.

(11) Shao, M.; Chang, Q.; Dodelet, J.-P.; Chenitz, R. Recent Advances in Electrocatalysts for Oxygen Reduction Reaction. *Chem. Rev.* **2016**, *116*, 3594−3657.

(12) Jung, N.; Chung, D. Y.; Ryu, J.; Yoo, S. J.; Sung, Y.-E. Pt-Based Nanoarchitecture and Catalyst Design for Fuel Cell Applications. *Nano Today* **2014**, *9*, 433−456.

(13) Chabot, V.; Higgins, D.; Yu, A.; Xiao, X.; Chen, Z.; Zhang, J. A Review of Graphene and Graphene Oxide Sponge: Material Synthesis and Applications to Energy and the Environment. *Energy Environ. Sci.* **2014**, *7*, 1564−1596.

(14) Jiang, H.; Zhu, Y.; Feng, Q.; Su, Y.; Yang, X.; Li, C. Nitrogen and Phosphorus Dual-Doped Hierarchical Porous Carbon Foams as Efficient Metal-Free Electrocatalysts for Oxygen Reduction Reactions. *Chem.—Eur. J.* **2014**, *20*, 3106−3112.

(15) Lin, Z.; Waller, G. H.; Liu, Y.; Liu, M.; Wong, C.-p. 3D Nitrogen-Doped Graphene Prepared by Pyrolysis of Graphene Oxide with Polypyrrole for Electrocatalysis of Oxygen Reduction Reaction. *Nano Energy* **2013**, *2*, 241−248.

(16) Liu, Z.; Nie, H.; Yang, Z.; Zhang, J.; Jin, Z.; Lu, Y.; Xiao, Z.; Huang, S. Sulfur-Nitrogen Co-Doped Three-Dimensional Carbon Foams with Hierarchical Pore Structures as Efficient Metal-Free Electrocatalysts for Oxygen Reduction Reactions. *Nanoscale* **2013**, *5*, 3283−3288.

(17) Wang, L.; Sofer, Z.; Ambrosi, A.; Šimek, P.; Pumera, M. 3D-Graphene for Electrocatalysis of Oxygen Reduction Reaction: Increasing Number of Layers Increases the Catalytic Effect. *Electrochem. Commun.* **2014**, *46*, 148−151.

(18) Wu, Z.-S.; Yang, S.; Sun, Y.; Parvez, K.; Feng, X.; Müllen, K. 3D Nitrogen-Doped Graphene Aerogel-Supported Fe3O4 Nanoparticles as Efficient Electrocatalysts for the Oxygen Reduction Reaction. *J. Am. Chem. Soc.* **2012**, *134*, 9082−9085.

DOI: 10.1021/acsami.9b04861
ACS Appl. Mater. Interfaces 2019, 11, 21526−21535

(19) Xue, Y.; Yu, D.; Dai, L.; Wang, R.; Li, D.; Roy, A.; Lu, F.; Chen, H.; Liu, Y.; Qu, J. Three-Dimensional B,N-Doped Graphene Foam as A Metal-Free Catalyst for Oxygen Reduction Reaction. *Phys. Chem. Chem. Phys.* **2013**, *15*, 12220−12226.
(20) Planeix, J. M.; Coustel, N.; Coq, B.; Brotons, V.; Kumbhar, P. S.; Dutartre, R.; Geneste, P.; Bernier, P.; Ajayan, P. M. Application of Carbon Nanotubes as Supports in Heterogeneous Catalysis. *J. Am. Chem. Soc.* **1994**, *116*, 7935−7936.
(21) Dou, S.; Li, X.; Tao, L.; Huo, J.; Wang, S. Cobalt Nanoparticle-Embedded Carbon Nanotube/Porous Carbon Hybrid Derived From MOF-Encapsulated Co_3O_4 for Oxygen Electrocatalysis. *Chem. Commun.* **2016**, *52*, 9727−9730.
(22) Serp, P. Carbon Nanotubes and Nanofibers in Catalysis. *Appl. Catal., A* **2003**, *253*, 337−358.
(23) Zhao, A.; Masa, J.; Xia, W.; Maljusch, A.; Willinger, M.-G.; Clavel, G.; Xie, K.; Schlögl, R.; Schuhmann, W.; Muhler, M. Spinel Mn-Co Oxide in N-Doped Carbon Nanotubes as A Bifunctional Electrocatalyst Synthesized by Oxidative Cutting. *J. Am. Chem. Soc.* **2014**, *136*, 7551−7554.
(24) Ma, Y.; Sun, L.; Huang, W.; Zhang, L.; Zhao, J.; Fan, Q.; Huang, W. Three-Dimensional Nitrogen-Doped Carbon Nanotubes/Graphene Structure Used as a Metal-Free Electrocatalyst for the Oxygen Reduction Reaction. *J. Phys. Chem. C* **2011**, *115*, 24592−24597.
(25) Lin, J.; Zhang, C.; Yan, Z.; Zhu, Y.; Peng, Z.; Hauge, R. H.; Natelson, D.; Tour, J. M. 3-Dimensional Graphene Carbon Nanotube Carpet-Based Microsupercapacitors with High Electrochemical Performance. *Nano Lett.* **2013**, *13*, 72−78.
(26) Sahoo, N. G.; Pan, Y.; Li, L.; Chan, S. H. Graphene-Based Materials for Energy Conversion. *Adv. Mater.* **2012**, *24*, 4203−4210.
(27) Yu, Y.-X. Can All Nitrogen-Doped Defects Improve the Performance of Graphene Anode Materials for Lithium-Ion Batteries? *Phys. Chem. Chem. Phys.* **2013**, *15*, 16819−16849.
(28) Ratso, S.; Kruusenberg, I.; Vikkisk, M.; Joost, U.; Shulga, E.; Kink, I.; Kallio, T.; Tammeveski, K. Highly Active Nitrogen-Doped Few-Layer Graphene/Carbon Nanotube Composite Electrocatalyst for Oxygen Reduction Reaction in Alkaline Media. *Carbon* **2014**, *73*, 361−370.
(29) Deng, J.; Ren, P.; Deng, D.; Bao, X. Enhanced Electron Penetration Through An Ultrathin Graphene Layer for Highly Efficient Catalysis of the Hydrogen Evolution Reaction. *Angew. Chem., Int. Ed.* **2015**, *54*, 2100−2104.
(30) Liu, Z.-Q.; Cheng, H.; Li, N.; Ma, T. Y.; Su, Y.-Z. ZnCo2 O4 Quantum Dots Anchored on Nitrogen-Doped Carbon Nanotubes as Reversible Oxygen Reduction/Evolution Electrocatalysts. *Adv. Mater.* **2016**, *28*, 3777−3784.
(31) Cheng, Y.; Dou, S.; Saunders, M.; Zhang, J.; Pan, J.; Wang, S.; Jiang, S. P. A class of transition metal-oxide@MnOx core-shell structured oxygen electrocatalysts for reversible O2 reduction and evolution reactions. *J. Mater. Chem. A* **2016**, *4*, 13881−13889.
(32) Dou, S.; Tao, L.; Huo, J.; Wang, S.; Dai, L. Etched and doped Co9S8/graphene hybrid for oxygen electrocatalysis. *Energy Environ. Sci.* **2016**, *9*, 1320−1326.
(33) Li, M.; Zhou, H.; Yang, W.; Chen, L.; Huang, Z.; Zhang, N.; Fu, C.; Kuang, Y. Co9S8nanoparticles embedded in a N, S co-doped graphene-unzipped carbon nanotube composite as a high performance electrocatalyst for the hydrogen evolution reaction. *J. Mater. Chem. A* **2017**, *5*, 1014−1021.
(34) Hou, Y.; Huang, T.; Wen, Z.; Mao, S.; Cui, S.; Chen, J. Metal−Organic Framework-Derived Nitrogen-Doped Core-Shell-Structured Porous Fe/Fe3 C@C Nanoboxes Supported on Graphene Sheets for Efficient Oxygen Reduction Reactions. *Adv. Energy Mater.* **2014**, *4*, 1400337−1400344.
(35) Liu, Y.; Li, J.; Li, W.; Li, Y.; Chen, Q.; Zhan, F. Nitrogen-doped graphene aerogel-supported spinel CoMn2O4 nanoparticles as an efficient catalyst for oxygen reduction reaction. *J. Power Sources* **2015**, *299*, 492−500.
(36) Guo, B.; Liu, Q.; Chen, E.; Zhu, H.; Fang, L.; Gong, J. R. Controllable N-Doping of Graphene. *Nano Lett.* **2010**, *10*, 4975−4980.
(37) Wei, J.; Liang, Y.; Zhang, X.; Simon, G. P.; Zhao, D.; Zhang, J.; Jiang, S.; Wang, H. Controllable Synthesis of Mesoporous Carbon Nanospheres and Fe-N/Carbon Nanospheres as Efficient Oxygen Reduction Electrocatalysts. *Nanoscale* **2015**, *7*, 6247−6254.
(38) Liu, Y.; Li, J.; Li, W.; Li, Y.; Zhan, F.; Tang, H.; Chen, Q. Exploring the nitrogen species of nitrogen doped graphene as electrocatalysts for oxygen reduction reaction in Al-air batteries. *Int. J. Hydrogen Energy* **2016**, *41*, 10354−10365.
(39) Jiao, Y.; Zheng, Y.; Jaroniec, M.; Qiao, S. Z. Origin of the Electrocatalytic Oxygen Reduction Activity of Graphene-Based Catalysts: A Roadmap to Achieve the Best Performance. *J. Am. Chem. Soc.* **2014**, *136*, 4394−4403.
(40) Li, F.; Chen, Z. Graphene-Based Materials as Nanocatalysts. *Graphene Chemistry: Theoretical Perspectives*; Wiley, 2013; pp 347−369.
(41) Chen, Z.; Yu, A.; Higgins, D.; Li, H.; Wang, H. Highly Active and Durable Core-Corona Structured Bifunctional Catalyst for Rechargeable Metal-Air Battery Application. *Nano Lett.* **2012**, *12*, 1946−1952.
(42) Boukhvalov, D. W.; Son, Y.-W. Oxygen reduction reactions on pure and nitrogen-doped graphene: a first-principles modeling. *Nanoscale* **2012**, *4*, 417−420.
(43) Odedairo, T.; Yan, X.; Ma, J.; Jiao, Y.; Yao, X.; Du, A.; Zhu, Z. Nanosheets Co3O4 Interleaved with Graphene for Highly Efficient Oxygen Reduction. *ACS Appl. Mater. Interfaces* **2015**, *7*, 21373−21380.
(44) Wu, J.; Gross, A.; Yang, H. Shape and Composition-Controlled Platinum Alloy Nanocrystals Using Carbon Monoxide as Reducing Agent. *Nano Lett.* **2011**, *11*, 798−802.
(45) Zhang, Y.; Ge, J.; Wang, L.; Wang, D.; Ding, F.; Tao, X.; Chen, W. Manageable N-Doped Graphene for High Performance Oxygen Reduction Reaction. *Sci. Rep.* **2013**, *3*, 2771.
(46) Mohamed, S. G.; Tsai, Y.-Q.; Chen, C.-J.; Tsai, Y.-T.; Hung, T.-F.; Chang, W.-S.; Liu, R.-S. Ternary Spinel MCo2O4 (M = Mn, Fe, Ni, and Zn) Porous Nanorods as Bifunctional Cathode Materials for Lithium-O2 Batteries. *ACS Appl. Mater. Interfaces* **2015**, *7*, 12038−12046.
(47) He, Q.; Li, Q.; Khene, S.; Ren, X.; López-Suárez, F. E.; Lozano-Castelló, D.; Bueno-López, A.; Wu, G. High-Loading Cobalt Oxide Coupled with Nitrogen-Doped Graphene for Oxygen Reduction in Anion-Exchange-Membrane Alkaline Fuel Cells. *J. Phys. Chem. C* **2013**, *117*, 8697−8707.
(48) Ju, Y.-W.; Yoo, S.; Kim, C.; Kim, S.; Jeon, I.-Y.; Shin, J.; Baek, J.-B.; Kim, G. Fe@N-Graphene Nanoplatelet-Embedded Carbon Nanofibers as Efficient Electrocatalysts for Oxygen Reduction Reaction. *Adv. Sci.* **2016**, *3*, 1500205−1500209.
(49) Bao, X.; Gong, Y.; Deng, J.; Wang, S.; Wang, Y. Organic-Acid-Assisted Synthesis of A 3D Lasagna-Like Fe-N-Doped CNTs-G Framework: An Efficient and Stable Electrocatalyst for Oxygen Reduction Reactions. *Nano Res.* **2016**, *10*, 1258−1267.
(50) Wei, C.; Wang, H.; Eid, K.; Kim, J.; Kim, J. H.; Alothman, Z. A.; Yamauchi, Y.; Wang, L. A Three-Dimensionally Structured Electrocatalyst: Cobalt-Embedded Nitrogen-Doped Carbon Nanotubes/Nitrogen-Doped Reduced Graphene Oxide Hybrid for Efficient Oxygen Reduction. *Chemistry* **2017**, *23*, 637−643.
(51) Niu, W.; Li, L.; Liu, X.; Wang, N.; Liu, J.; Zhou, W.; Tang, Z.; Chen, S. Mesoporous N-Doped Carbons Prepared with Thermally Removable Nanoparticle Templates: An Efficient Electrocatalyst for Oxygen Reduction Reaction. *J. Am. Chem. Soc.* **2015**, *137*, 5555−5562.
(52) Liu, Y.; Jiang, H.; Hao, J.; Liu, Y.; Shen, H.; Li, W.; Li, J. Metal-Organic Framework-Derived Reduced Graphene Oxide-Supported ZnO/ZnCo2O4/C Hollow Nanocages as Cathode Catalysts for Aluminum-O2 Batteries. *ACS Appl. Mater. Interfaces* **2017**, *9*, 31841−31852.

DOI: 10.1021/acsami.9b04861
ACS Appl. Mater. Interfaces 2019, 11, 21526−21535

(53) Tong, X.; Chen, S.; Guo, C.; Xia, X.; Guo, X.-Y. Mesoporous NiCo2O4 Nanoplates on Three-Dimensional Graphene Foam as an Efficient Electrocatalyst for the Oxygen Reduction Reaction. *ACS Appl. Mater. Interfaces* **2016**, *8*, 28274−28282.
(54) Meng, Y.; Song, W.; Huang, H.; Ren, Z.; Chen, S.-Y.; Suib, S. L. Structure-Property Relationship of Bifunctional MnO2 Nanostructures: Highly Efficient, Ultra-Stable Electrochemical Water Oxidation and Oxygen Reduction Reaction Catalysts Identified in Alkaline Media. *J. Am. Chem. Soc.* **2014**, *136*, 11452−11464.
(55) Lu, Y.-F.; Lo, S.-T.; Lin, J.-C.; Zhang, W.; Lu, J.-Y.; Liu, F.-H.; Tseng, C.-M.; Lee, Y.-H.; Liang, C.-T.; Li, L.-J. Nitrogen-Doped Graphene Sheets Grown by Chemical Vapor Deposition: Synthesis and Influence of Nitrogen Impurities on Carrier Transport. *ACS Nano* **2013**, *7*, 6522−6532.
(56) Ardizzone, S.; Bianchi, C. L.; Tirelli, D. Mn3O4 and γ-MnOOH powders, preparation, phase composition and XPS characterisation. *Colloids Surf., A* **1998**, *134*, 305−312.
(57) Davis, D. J.; Lambert, T. N.; Vigil, J. A.; Rodriguez, M. A.; Brumbach, M. T.; Coker, E. N.; Limmer, S. J. Role of Cu-Ion Doping in Cu-α-MnO2 Nanowire Electrocatalysts for the Oxygen Reduction Reaction. *J. Phys. Chem. C* **2014**, *118*, 17342−17350.
(58) Zhao, Y.; Yang, X.; Kuo, L.-Y.; Kaghazchi, P.; Sun, Q.; Liang, J.; Wang, B.; Lushington, A.; Li, R.; Zhang, H.; Sun, X. High Capacity, Dendrite-Free Growth, and Minimum Volume Change Na Metal Anode. *Small* **2018**, *14*, 1703717−1703724.
(59) Ma, T. Y.; Zheng, Y.; Dai, S.; Jaroniec, M.; Qiao, S. Z. Mesoporous MnCo2O4with abundant oxygen vacancy defects as high-performance oxygen reduction catalysts. *J. Mater. Chem. A* **2014**, *2*, 8676−8682.
(60) Kaukonen, M.; Kujala, R.; Kauppinen, E. On the Origin of Oxygen Reduction Reaction at Nitrogen-Doped Carbon Nanotubes: A Computational Study. *J. Phys. Chem. C* **2011**, *116*, 632−636.
(61) Liu, Y.; Sun, Q.; Yang, X.; Liang, J.; Wang, B.; Koo, A.; Li, R.; Li, J.; Sun, X. High-Performance and Recyclable Al-Air Coin Cells Based on Eco-Friendly Chitosan Hydrogel Membranes. *ACS Appl. Mater. Interfaces* **2018**, *10*, 19730−19738.

DOI: 10.1021/acsami.9b04861
ACS Appl. Mater. Interfaces 2019, 11, 21526−21535